Chemical Engineering Journal 427 (2022) 132028

Contents lists available at ScienceDirect

Chemical Engineering Journal

journal homepage: www.elsevier.com/locate/cej

Electronic and thermal transfer actuating memory catalysis for organic removal by a plasmonic photocatalyst

Futao Yi [a], Jianqing Ma [a,b,*], Chuanwei Lin [a], Huining Zhang [a,b], Yongxing Qian [a,b], Huixia Jin [a,b], Kefeng Zhang [a,b]

[a] School of Civil Engineering and Architecture, NingboTech University, Ningbo 315100, China
[b] Ningbo Research Institute, Zhejiang University, Ningbo 315100, China

ARTICLE INFO

Keywords:
Plasmon
Thermal conversion
Electron transfer
Memory catalysis

ABSTRACT

To take full advantage of solar energy, a memory-catalyst Ag/BiOCl/Ti_3C_2 was fabricated using a two-step precipitation method, which performed well in the degradation of tetracycline hydrochloride (TC) in the light and dark. The generation of reactive oxygen species in the light and dark were both certified. Furthermore, quenching experiments and quantum lifetime measurements demonstrated the excited-electron transfer process, and these tests confirmed the electron (e^-) transformation resulting from the localized surface plasmon resonance effect (LSPR) in two-electron donors, Ag NPs and Ti_3C_2.Further, the calculation using COMSOL software suggested the enhancement of the electric field through modification of the two co-catalysts mentioned above. Because of this enhancement, the activated e^- might be further reacted in the dark for the memory-catalysis process. On the other hand, based on the result of IR thermal imaging, the thermal transmission for formation using LSPR might be another factor in promoting memory catalysis as an energy resource. This work demonstrates for the first time that LSPR might actuate memorycatalysis using e^- transmission and energy input, and the results shed light on the design and comprehension of memory photocatalysis for its practical use in pollutant removal and other fields.

1. Introduction

Powered by free, clean, and sustainable solar energy, photocatalysis offers a promising strategy to solve energy and environmental issues. In recent decades, photocatalysis has made great advances in many fields, such as pollutant removal, disinfection [1], hydrogen production [2], and organic synthesis [3]. Many improvements have been made in the efficient utilization of solar energy. For example, the latest photocatalyst can harvest a full range of the spectrum from ultraviolet (UV) to near-infrared light. However, there is still a long way to go before its extensive application, because photocatalysis is always activated by light and consequently subject to weather and light conditions.

To make the photocatalyst more active and efficient in various situations, researchers have put forward the so-called "all-day-active photocatalyst," "round-the-clock photocatalyst" (RTCPt) [4], and "memory catalyst" (MC) [5]. The principle behind these photocatalysts is that certain energy-storage materials would allow the photocatalysts to react even in the dark [6]. Thus, some materials that are used in batteries and supercapacitors are composited with photocatalysts [7–9]. Metallic silver (Ag), widely used in batteries because of its strong conductivity and electron-storing ability, is a strong candidate for use in memory catalysis [10–12]. Choi *et al.* suggested that Ag nanoparticles (NPs) could facilitate a sequential process reaction for photocatalytic oxidation of organic pollutants and dark reduction with Cr (VI), through the e^- release of Ag NPs in the dark [13]. Carbon-based materials play a vital role in supercapacitors and could be another promising candidate for MC [14–16]. Titanium carbide (Ti_3C_2), known for its remarkable characteristics of e^- deposition and electronegativity, is a typical carbon-based Mxenes material [17,18]. In the photocatalysis field, Ti_3C_2 acted as an outstanding co-catalyst to form a Schottky junction, which can enhance the transmission of charge carriers and light availability [19,20]. Predictably, Ti_3C_2 will shine in the field of memory catalysis owing to its unique electronic properties and photocatalytic activity. Its precise mechanism to actuate MC is worthy of further exploration.

It is reported that both Ti_3C_2 and Ag can induce a localized surface plasmons response (LSPR). This suggests that memory catalysis could be

* Corresponding author at: School of Civil Engineering and Architecture, NingboTech University, Ningbo 315100, China.
E-mail address: majq@nit.zju.edu.cn (J. Ma).

https://doi.org/10.1016/j.cej.2021.132028
Received 21 April 2021; Received in revised form 10 August 2021; Accepted 21 August 2021
Available online 25 August 2021

induced through another mechanism. Little attention has been paid to the energy and charge carriers produced by LSPR for memory catalysis. However, it might prove effective in improving the activity of MC, because the charge carriers generated by the non-radiative decay of LSPR were more energetic than photo-excited charge carriers [21,22]. LSPR might contribute two main synergistic effects to enhance photocatalytic activity. First, after thermal excitation, the hot-electron might be discrete through the transformative pathway of $\sigma \rightarrow \sigma^*$ mode, which facilitates the response of light in the visible and infrared regions, and therefore contributes more energy to exciting charge carriers than the original catalyst [23–25]. The thermal contribution to plasmonic photocatalysis by Ag and Au NPs has been well documented in a previous study [21]. Additionally, IR thermal images demonstrated that the Ti_3C_2/Ag NPs emerged as a thermal effect because of the plasmonic photocatalysis from Ag and photo-thermal effects resulting from Ti_3C_2 [26]. Fan *et al.* also demonstrated the LSPR from Ti_3C_2 induced thermal effect [27]. Another enhanced mechanism can be attributed to the charge carriers transfer from plasmas to semiconductors, which prolongs the quantum lifetime and leads to some photocatalytic reaction on the surface of the semiconductors [28–30]. The competitive relationship between these two effects, and the stimulation of molecular dynamics, is also demonstrated in Zhang *et al.* [31].

The present work aims to utilize the LSPR effect to actuate memory photocatalysis performance in organics removal. BiOCl is a strong semiconductor photocatalyst with tunable optical absorption and layered nanosheets structure when composited with Ag NPs or Ti_3C_2. This heterojunction can be constructed and a resonant electric field will be generated using LSPR with the migration of Fermi level between Ag NPs or Ti_3C_2 with BiOCl. Therefore, a memory catalyst Ag/BiOCl/Ti_3C_2 was fabricated and its impressive catalytic property for tetracycline hydrochloride degradation, in both the light and dark, was verified. Based on the quantum lifetime and electron-donor performance resulting from Ti_3C_2 and Ag NPs, the mechanism of the plasmonic charge carrier transfer channel via Ti_3C_2 and Ag NPs to BiOCl was confirmed. Another simulative mechanism with thermal conversion was put forward using thermal imaging and COMSOL calculation. These results provide new insight into the design and understanding of MC and plasmonic photocatalysis.

2. Materials and methods

2.1. Catalysts preparation

All agents were analytical grade and purchased from Sinopharm Chemical Reagent Co. Ltd, without further treatment. First, the Ti_3C_2 was synthesized using acid exfoliation and a handshake method [32]. Then, 2.134 g $Bi(NO_3)_3{\cdot}5H_2O$ and 0.30 g as-prepared Ti_3C_2 powder were both added to 50 mL deionized water. After stirring for 20 min, 0.25 mL HCl was dropped into the suspension and stirred for 45 min at 60 °C. The obtained sample was washed several times and dried in a vacuum oven. The pure BiOCl was fabricated by the process same as BiOCl/Ti_3C_2 except for the involvement of Ti_3C_2. Then, the metallic Ag was composited with the BiOCl/Ti_3C_2 using the light-deposition method [33]. $AgNO_3$, as the silver source, was mixed with BiOCl/Ti_3C_2 in the alcohol solution (volume ratio = 20%) and dispersed in the dark for 30 min. Finally, the homogeneous suspension was irradiated under a 300 W Xe lamp without a cutoff to reduce Ag^+ on the sample surface. The sample of Ag/BiOCl was prepared by the same steps except that BiOCl was substituted for BiOCl/Ti_3C_2. The separative and drying process was the same as the treatment above.

2.2. Characterization methods

Powder X-ray diffraction patterns (XRD) of as-prepared powders were scanned from 5° to 90° using a D8 Advance X-Ray diffractometer (Bruker AXSGmbH, Germany) with Cu Kα radiation. X-ray photoelectron spectroscopy (XPS) was studied using an Escalab 250XI spectrometer (Thermo Fisher Scientific, USA) using calibration C 1 s at 284.8 eV. A Merlin scanning electron microscope (SEM; Zeiss Microscopy, Germany) and a Libra 200FE high-resolution transmission electron microscope (HRTEM; Zeiss Microscopy, Germany) were used to study the morphology of as-prepared samples, and energy dispersive X-ray spectroscopy (EDS, Zeiss Microscopy, Germany) gave the element analysis of the samples. All fluorescence spectra were obtained using an FL3-111 fluorescence spectrophotometer (HORIBA, Ltd., Japan) with excitation light at 384 nm. The optical absorbance and refraction capability of the as-prepared sample was tested using the UV/vis/NIR spectrometer (Lambda 950, PerkinElmer, Inc., USA). Specifically, 10.0 mg catalyst was dispersed in the 3.0 mL deionized water and then the suspension was transferred into the quartz cell for absorption spectra measurement. The IR thermal imaging was conducted using a S65 thermal infrared imager (FLIR Systems, Inc., USA).

2.3. Performance tests of the catalysts

Photocatalytic and MC activity was tested by removing TC in both the light and dark. To evaluate the photocatalytic performance, the as-prepared sample (0.1 g/L) was dispersed in the TC solution (10 mg/L) and stirred in dark for 60 min. Then, the mixture was irradiated using an Xe lamp (PLS-SXE300D, Beijing Perfect light Technology Co., Ltd.) with a cut filter (λ>420 nm) at room temperature. The irradiation intensity is 143 mW/m^2. Moreover, a recycle water system was used to keep the room temperature. After a certain length of time interval, the sample was removed and quantified using a UV/vis spectrometer at 357 nm. To evaluate the MC activity, the catalysts were added to deionized water and stirred constantly for 150 min under a Xe lamp. After that, the light was turned off, and TC was dispersed into the suspension. After a certain length of time, the sample was removed and quantified using the method mentioned above. As the blank control, the adsorption test in the dark was also conducted without the previous light irritation.

Reactive oxygen species (ROS) generation during the reactions was determined using electron spin resonance (ESR) signals on an electron paramagnetic resonance spectrometer (ER200-SRC, Bruker AXSGmbH, Germany). The samples were removed at 4 min and 8 min, and immediately mixed with 5, 5-Dimethyl-1-pyrroline N-oxide (DMPO) solution for •OH (in water) and $\bullet O_2^-$ (in methanol) detection.

2.4. Exploring the memory catalysis mechanism

The transient photo-current experiment used a CHI 630E electrochemical workstation with a three-electrode cell in two different ways. In the short-term detection, the electrode was immersed in pure Na_2SO_4 (2 M) or the mixture containing Na_2SO_4 and *N, N*-methyviologen ions (MV^{2+}, 0.1 mM) during the measurement of the current response. Another test with long-term detection was conducted for the MC. The step was executed as follows: First, the intensity of current was detected under the irradiation of UV light for 30 min. Second, the test was started in the dark to measure the response of the current.

To test the photothermal effect from the catalyst, the degradative reaction was conducted under different temperatures (298 K, 303 K, 308 K) through a water bath, the other details were the same as the performance test of the catalyst.

2.5. The quenching experiment

To determine the capacity of electron-donating and accepting, the MV^{2+} quantitative quenching method [34] was used. In detail, the stock quencher (*N, N*-methyviologen (MV)) solution was diluted to a range between 0.01 M and 0.1 M. Then, 0.1 g catalyst was added to this serial of 50 mL solutions with different concentrations. The suspension was dispersed by ultrasonic treatment. This homogeneous suspension was detected upon the excitation at 384 nm.

2.6. Finite element simulation

The numerical model was simulated using the three-dimensional, finite element method (3D-FEM; commercial software package, COMSOL Multiphysics 5.0). The whole volume for simulation was 1 μm ×1 μm ×1 μm, and the medium in the space was air. The incident light irradiated the materials from the top margin to the bottom boundary. At the center of the space was the BiOCl semisphere (D = 500 nm), which was located on the Ti_3C_2 sheets (1 μm ×1 μm ×0.1 μm). The Ag NPs were deposited on the BiOCl surface. Moreover, the vector wave equation was solved for the time-harmonic electric field:

$$\nabla \times (\nabla \times E) - k_0^2 \varepsilon_r E = 0 \quad (1)$$

$$\varepsilon_r = (n - ik)^2, \sigma = 0, \mu_r = 1 \quad (2)$$

Where ε_r is the relative permittivity; (E = Ex, Ey, Ez) is the electric field; and $k_0 = 2\pi/\lambda$ is the incident wave vector with λ as the wavelength of the incident plane wave. Moreover, the refractive index of Ti_3C_2 is −4.66 and -3.47×10^{-20} m^2/W at 800, 1064 nm, respectively [35]. And the dielectric constant of BiOCl and Ag NPs are 4.61, 0.68, respectively [36,37].

3. Results and discussion

3.1. 3.1.Heterojunction construction and its optical characteristics

First, the morphology and chemical structures of the as-prepared samples were analyzed. As shown in SEM (Fig. S1) and HRTEM (Fig. 1) images, pristine BiOCl nanosheets were stacked to form the flower-like microspheres. Its diffraction peaks at 11.9°, 25.7°, 32.6°, and 33.5°, were identical with the (001), (101), (110), and (102) planes of tetragonal phase BiOCl (JCPDS: 06-0249). When composited with Ti_3C_2, these flower-like structures were located on the flat Ti_3C_2 layers (Fig. S1d). The morphology graph suggests a solid interaction between BiOCl and Ti_3C_2. The diffraction peak at 36.0° corresponds to the Ti_3C_2 structure prepared using the Ti_3AlC_2 etching method [38], while the peak at 24.3° was contributed to the partially oxidized Ti_3C_2. After the photo-deposition, Ag nanoparticles (represented by the yellow dot in Fig. 1c) with several dozens of nanometers were deposited on the surface of BiOCl structure (Fig. S1f), and new diffraction peaks emerged at 38.2°, 44.4°, and 64.6°, which can be ascribed to the (111), (200), and (220) crystal planes of metallic Ag (JCPDS: 04-0783). The sample obtained exhibited all of the characteristic peaks typical of BiOCl, Ti_3C_2, and Ag, indicating the successful construction of an Ag/BiOCl/Ti_3C_2 heterojunction. Additionally, as shown by the red line, the lattice spacing in Fig. 1d was 0.203 nm and was well-matched with the metallic Ag (200) crystal facet, further confirming the existence of Ag NPs on the sample surface. Element contents were calculated using EDS and shown in Table S1.

XPS measurement was used to detect the chemical state of different elements in Ag/BiOCl/Ti_3C_2. All signals of Bi, Cl, C, Ti, O, and Ag were observed in the composite sample (Fig. 2 and Fig. S2). The spectrum of Bi 4f displayed a characteristic of Bi^{3+}. Based on the peak at the Bi 4f and Cl 2p spectrum, the successful fabrication of the BiOCl could be confirmed. The spectrum of O 1 s can be divided into lattice oxygen of BiOCl and Ti_3C_2, adsorbed oxygen, and adsorbed hydroxyl groups on the composite surface. The emergence of C was the result of the Ti_3C_2 component and the introduction of the XPS measurement. The Ti 2p spectrum overlapped with Bi $4d_{3/2}$, thus a broad peak formed at about 461 eV. However, a peak at 454.0 eV which is much lower than that of $2p_{3/2}$ of Ti-O bond (458.3 eV) can be ascribed to the Ti-C bond [39,40]. The Ag $3d_{3/2}$ and Ag $3d_{5/2}$ peaks at 368.3 eV and 374.3 eV, with the relevant loss feature on their higher binding energy side, further suggest the existence of metallic Ag in the Ag/BiOCl/Ti_3C_2 sample [41]. This low valence state might hold strong reductive activity and act as an electron donor in the photocatalytic reaction.

The optical absorbance of as-prepared samples in Fig. 3 was characterized using UV-vis diffuse reflectance spectra. According to *Eq.*3 and Tauc plot [42,43], the calculated for bidden gaps

$$E_g = (\alpha h\nu)^n \quad (3)$$

of BiOCl was 3.13 eV. According to the previous report [44], the modification by co-catalysts could not affect the band gap. On the other hand, as shown in Fig. 3a, co-catalyst contributed much enhancement in optical absorbance. This result demonstrated that the constructed heterojunction could narrow the bandgap and thus facilitate the response to light. Moreover, when composited with Ti_3C_2 and Ag, the intensity of light absorbance was dramatically enhanced at a wide range as a result of the localized surface plasmon resonance (LSPR). The obvious absorbance peak, located around 470 nm, suggests that the transversal LSPR was caused by metallic Ag NPs [12,45]. This peak arose from the plasmon resonance generated using the excess electrons at Ag 5p orbital [46]. Although the plasmonic peak of MXene materials was not obvious, the enhancement of light absorbance could be contributed to the plasmonic band of MXene materials. In summary, the effect of transversal

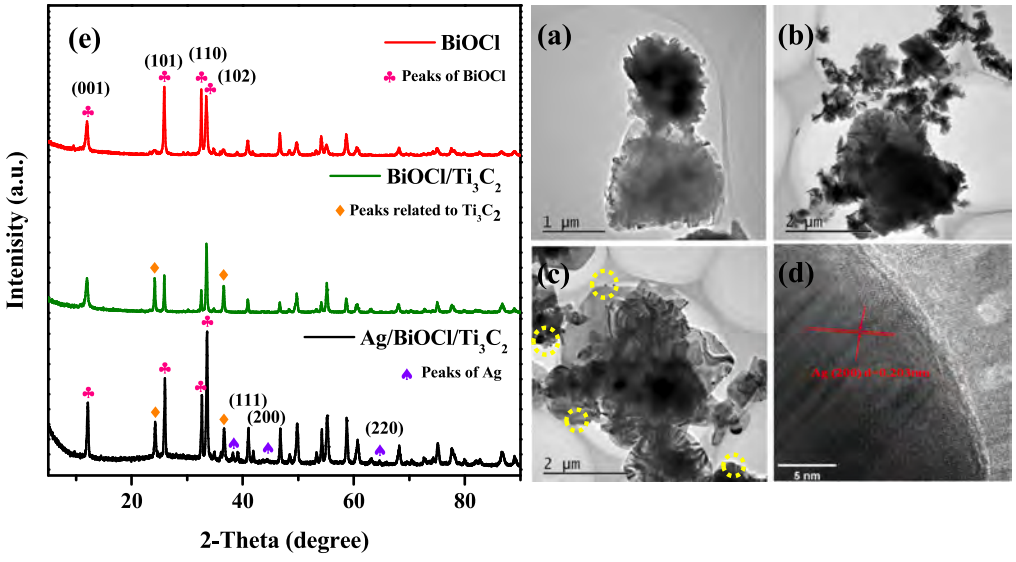

Fig. 1. HRTEM images of the prepared (a) BiOCl, (b) BiOCl/Ti_3C_2, (c) and (d) Ag/BiOCl/Ti_3C_2 samples; (e) XRD patterns of as-prepared samples.

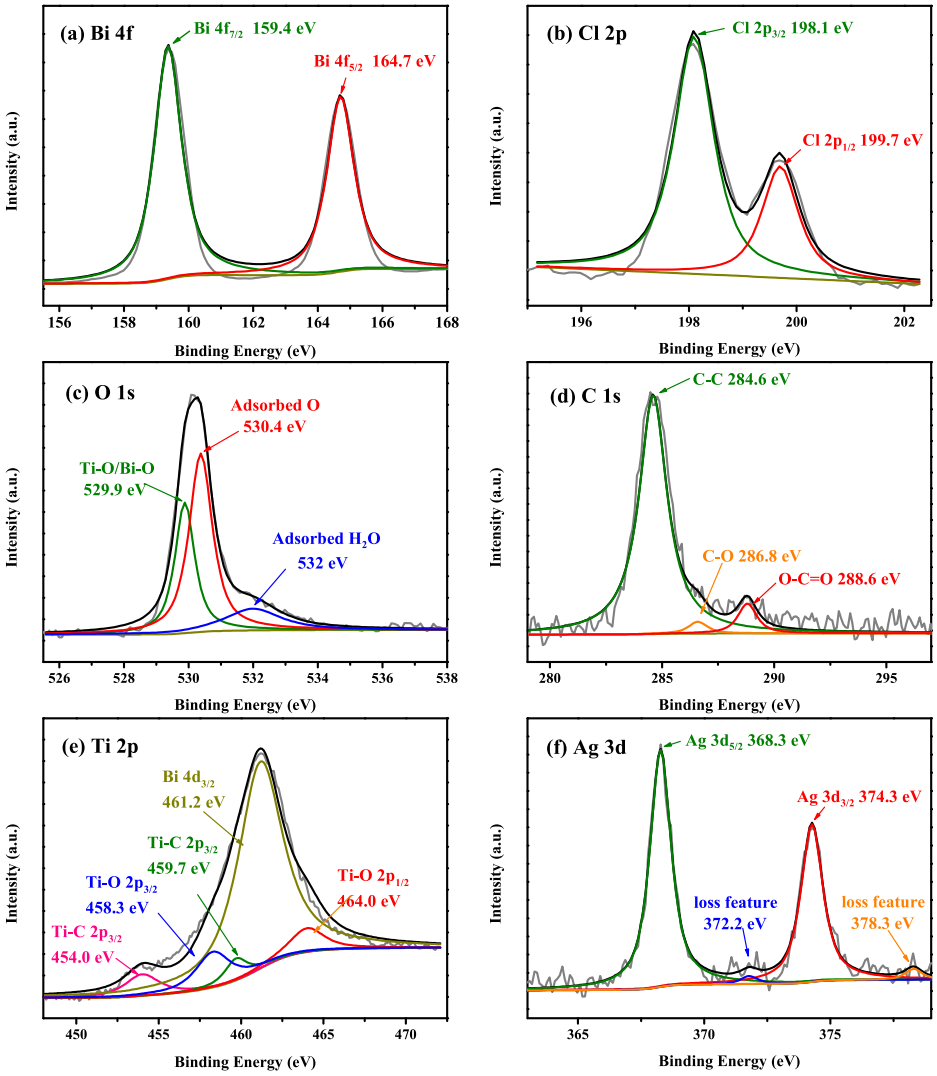

Fig. 2. XPS spectra of Ag/BiOCl/Ti_3C_2: (a) Bi 4f; (b) Cl 2p; (c) O 1 s; (d) C 1 s; (e) Ti 2p and (f) Ag 3d.

and longitudinal LSPR generated through Ag NPs and Ti_3C_2 nanosheets could further enhance the light excitation. In addition, the curve of Ag/BiOCl/Ti_3C_2 displayed little difference with BiOCl/Ti_3C_2 and suggests a strong plasmonic coupling between Ag NPs and BiOCl/Ti_3C_2 through the variety of dipoles. Another effect of the enhanced LSPR effects was provided by reflection spectra (Fig. 3c). An obvious enhancement of reflectance intensities by modification of Ti_3C_2 and Ag NPs was observed. The peak located at 480 nm is the result of the LSPR effect from Ag NPs [27,47]. Moreover, according to the previous report and transfer matrix theory [48,49], the LSPR effect from Ag NPs could improve the optical reflectance performance. However, due to the low content of Ag, the peak might be covered by the enhancement of reflectance from Ti_3C_2 and therefore not obvious in this study. Finally, the peak at the 1900 nm might be attributed to the reflectance of water. In conclusion, the plasmonic polarization from above two co-catalysts promotes the stored charge carriers transfer by the photo-electric process.

3.2. Catalytic performance in the light and dark

As an antibiotic that is used extensively worldwide, tetracycline hydrochloride was chosen as a model pollutant to evaluate memory catalytic performance. Fig. 4a shows that the removal efficiency of BiOCl, Ag/BiOCl, BiOCl/Ti_3C_2, and Ag/BiOCl/Ti_3C_2 under visible light was 37.7%, 91.2%, 92.0%, and 97.9%, respectively. The UV-visible absorption spectra in Fig. S3 verified that TC almost disappeared in 60 min in the Ag/BiOCl/Ti_3C_2 system, while a certain amount of TC still remains for BiOCl. Moreover, in the ternary composite system, the adsorption played a minor role during the pollutant removal process. Clearly, the heterojunction of Ag/BiOCl/Ti_3C_2 improved the photocatalytic degradation activity of organic removal. As mentioned in a previous study, the photocatalytic degradation reaction was usually fitted to the pseudo-first-order reaction kinetics [7]. However, the k (kinetics constant) value (Table S2) over the composite sample displayed low fitness for the original reaction model, and the R^2 of the fitted curves was only 0.9087 (Fig. S4). The Langmuir-Hinshelwood kinetics model can describe the photocatalytic degradation of organic pollutants at the liquid-solid interface with the calculation as following [50]:

$$t = \left(\frac{1}{KK_r}\right) Ln\left(\frac{C_0}{C}\right) + \frac{C_0 - C}{K_r} \quad (4)$$

$$k_{app} = KK_r \quad (5)$$

where t refers to the irradiation time, C_0 (mg/L) is the initial concentration of TC and C (mg/L) is the concentration of the pollutant at time t, K is the equilibrium constant for the pollutant adsorption on the catalyst and K_r reflects the limiting rate of the reaction at the maximum coverage under the given conditions. The k_{app} is the apparent constant. It

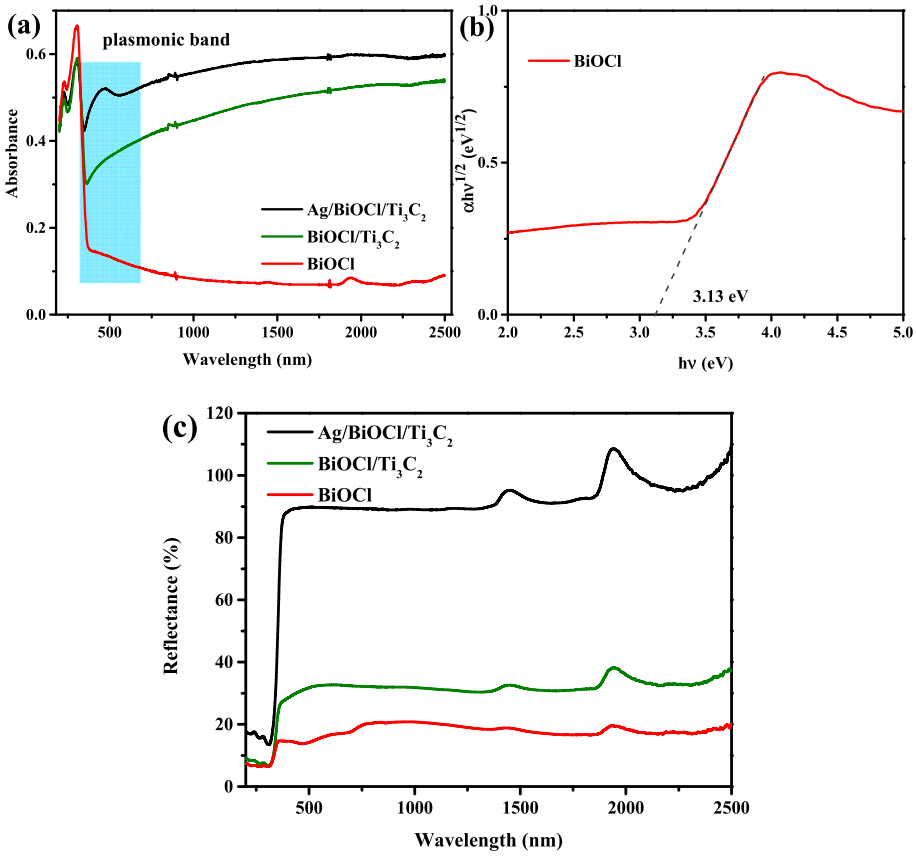

Fig. 3. (a) UV–vis absorbance spectra of BiOCl, BiOCl/Ti_3C_2 and Ag/BiOCl/Ti_3C_2, and (b) Tauc plot of BiOCl, (c) reflection spectra of as-prepared samples.

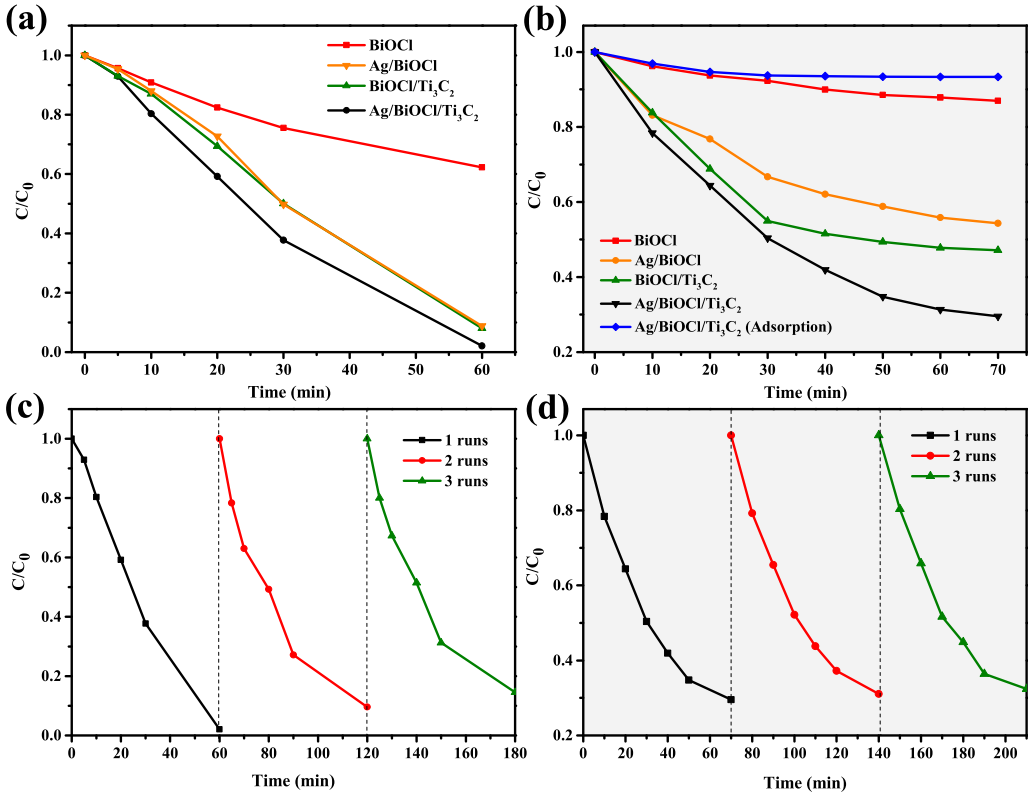

Fig. 4. (a) Light and (b) dark removal of TC by as-prepared samples; (c) successive cycle for (c) the light and (d) the dark removal of TC (catalyst dosage 0.1 g/L; TC 10 mg/L).

indicated that the reaction process with the modified catalyst was well-fitted with the Langmuir-Hinshelwood kinetics model (R^2 >0.99) (Fig. S4). According to the results in Table S2, the Ag/BiOCl/Ti_3C_2 displayed over 60 times enhancements in photocatalytic ability compared with BiOCl.

After light irradiation, all catalysts except BiOCl continued to display remarkable catalytic activity in the dark (Fig. 4b). The removal efficiency for BiOCl, Ag/BiOCl, BiOCl/Ti_3C_2, and Ag/BiOCl/Ti_3C_2 after 70 min was 13.1%, 45.7%, 52.8%, and 70.5%, respectively. Not surprisingly, Ag/BiOCl/Ti_3C_2 performed best among all modified samples. The adsorption test revealed that only 6.7% of TC was removed without light irradiation beforehand, thus confirming that TC mostly declined as the result of degradation rather than adsorption. It can be concluded from these results that the combination of Ti_3C_2 and Ag was an efficient method to improve the photocatalytic activity of BiOCl, whether in the dark or light. ROS might still be generated after light irradiation, implying the great potential use of Ag/BiOCl/Ti_3C_2 for memory catalysis.

Stability and recyclability are important properties for the application of a photocatalyst, thus three successive degradation experiments in the light and dark were conducted. Fig. 4c and d shows, after three cycles, only a slight decay in photocatalysis. In detail, the removal rate only decreased from 97.9% to 85.5% for light degradation, and the dark eliminative rate decreased from 70.5% to 69.2%. Both of these results indicate that Ag/BiOCl/Ti_3C_2 is stable and renewable.

3.3. Reactive oxygen species determination

The trapping experiments and ESR spectra were conducted to determine the generation of ROS in the reactions. EDTA-2Na, $AgNO_3$, and isopropanol (IPA) were employed to act as scavengers for h^+, e^- and hydroxyl radicals, respectively. Fig. 5a and b show that the addition of EDTA-2Na carried much decay of the light degradation (97.9–49.5%), whereas the effect using the same trapping agent could be ignored in the dark (70.5–66.1%). It suggests that the photo-excited holes (h^+) played vital roles, corresponding to the light and dark elimination. On the other hand, obvious inhibitions appeared in both light (inhibition rate 35.2%) and dark (inhibition rate 45.7%) after the addition of $AgNO_3$. This reduction indicates that e^- might be the significant species in both conditions. For IPA, a large reduction in TC degradation was also noticeable, indicating the existence of a hydroxyl radical (•OH) in the above two photocatalytic systems [15,50].

ESR spectra further confirmed the existence of $\bullet O_2^-$ in the two reaction systems mentioned above. Based on the characteristic signal

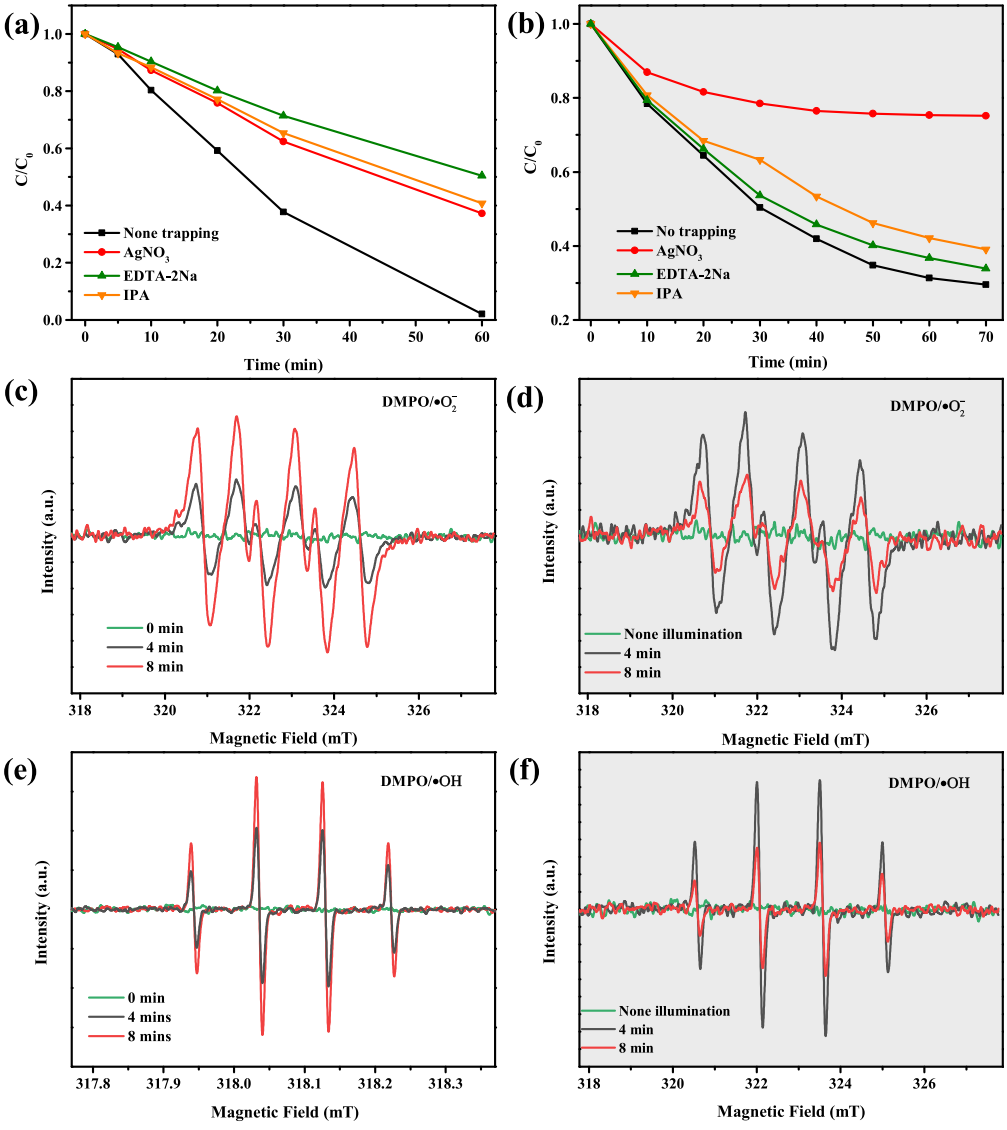

Fig. 5. Trapping experiment: (a) in the light and (b) in the dark; ESR spectra of Ag/BiOCl/Ti_3C_2:(c and d) under irradiation and (e and f) after irradiation.

peaks in Fig. 5c–f, both $\bullet O_2^-$ and •OH occurred and were generated in the light and dark [15,34]. However, the change of peak intensity in two different systems led to the opposite trend. Specifically, the intensity of the signal peak increased with a longer time in the light whereas it decreased in the dark with the extension of determination time. The outline of the degradation mechanism was beginning to become clear: under light, h^+ and e^- were generated on the catalyst surface, followed by $\bullet O_2^-$ and •OH [19]. The lifetime of $\bullet O_2^-$ and •OH is transient, consequently it can be deduced that, when the light is turned off, $\bullet O_2^-$ and •OH continued to form, mainly using the following pathway [51]:

$$e^- + O_2 \rightarrow \cdot O_2^- \quad (6)$$

$$O_2^- + e^- + 2H^+ \rightarrow H_2O_2 \quad (7)$$

$$O_2^- + H_2O_2 \rightarrow \cdot OH + OH^- + O_2 \quad (8)$$

$$H_2O_2 \rightarrow 2 \cdot OH \quad (9)$$

As the stored e^- was consumed, the generated $\bullet O_2^-$ and •OH decreased, causing an evident reduction in the peak intensity. Therefore, oxidized using h^+ (only in the light), $\bullet O_2^-$, and •OH, TC in the solution was degraded. The specific degradation pathways oxidized by these ROS are shown in Text S1, Figs. S5 and S6.

3.4. Exploration of the plasmonic mechanism

3.4.1. The transmission of excited electrons between the co-catalysts and BiOCl

In the mechanism mentioned above, co-catalysts seem only to have played a role in the storage and release of the photo-induced electron as mentioned in previous studies [13], however, more details, such as the plasmonic effect, need to be deciphered to give a comprehensive overview of the mechanism that drove the efficient ROS generation in both the light and dark in this study. The production process of excited e^- in the light and dark was first checked using the photo-current response. Fig. 6a shows that the long-term measurement of photo-current revealed that the best conductivity was achieved using Ag/BiOCl/Ti_3C_2 among all as-prepared samples as a result of its best separative feature photo-excited electron-hole pairs [33]. It is worth noting that a delayed recession appeared in the sample composed with Ti_3C_2 and Ag NPs after the light was turned off, confirming that the co-catalysts, Ti_3C_2 and Ag NPs might be storage or supercapacitor to reserve excited e^- for the later generation of ROS in the dark [52]. To detect the property of a donor-acceptor (D-A) system existing in the as-fabricated samples, the short-term, photo-current response was tested in a different aquatic environment. Fig. 6b shows that MV^{2+}, a well-known electron-acceptor, was introduced to build the system mentioned above [34,53]. This complex solution greatly enhanced photo-current response with the test of a modified sample compared with that without MV^{2+}. This further indicates that the donative property of excited electrons, generated using the co-catalyst Ti_3C_2 and Ag NPs, was contributed by the surface excited-electron density. In summary, the measurement of photo-current response using two different modes suggests that the modification using Ag NPs and Ti_3C_2 could reserve and provide excited-electrons to support the photocatalytic degradation.

It is reported that the separation of electron-hole pairs could provide more reactive species to take part in the reaction and prolong the quantum lifetime [19]. Fig. 7a shows the declining peak from the steady PL spectra of Ag/BiOCl/Ti_3C_2, indicating the introduction of both Ti_3C_2 and Ag NPs could boost the separation of excited electron-hole pairs, as a result of the electron transmission activated using the Schottky junction [54,55]. In detail, because of the difference between the Fermi level of BiOCl ($\varphi = 1.98$ V vs. NHE), Ag ($\varphi = 0.32$ V vs. NHE) [56], and Ti_3C_2 ($\varphi = 0.79$ V vs. NHE) [57], the Schottky junction was fabricated between the main component and co-catalysts. The results show that the Fermi level of the main component and co-catalyst are in balance, which delivers a Schottky barrier that promotes the excited e^- shift from Bi 6p orbital (BiOCl) to d band of Ag NPs and Ti_3C_2 as an interchange. After the plasmonic excitation, these transferred e^- shifted to Ag 5p orbital (Ag NPs) and Ti 2p orbital (Ti_3C_2) as plasmonic-charge carriers [40,56,58]. Based on results from the time-resolved PL spectra in Fig. 7b, the quantum lifetime was calculated using the two-parameter equation [19]:

$$\tau_{average} = \sum_{i=1}^{2} A_i \tau_i^2 / \sum_{i=1}^{2} A_i \tau_i \quad (10)$$

The quantum lifetime of Ag/BiOCl/Ti_3C_2 (34.63 ns) was also much longer than BiOCl (11.77 ns) and BiOCl/Ti_2C_3 (14.86 ns) all data are shown in Table S3). The first lifetime could be attributed to the defect trapping to the exciton in catalyst and the second lifetime is related to the relaxation of excited charge carriers [59]. In the as-prepared sample, BiOCl is the main content and a few co-catalysts are modified on the surface of the catalyst. Moreover, the defect in BiOCl is limited. Therefore, the first lifetime seems not much affected by Ag NPs and Ti_3C_2, but this modification provides new pathways for electrons relaxation. As the result, the second lifetime prolongs distinctively by Ti_3C_2 and Ag NPs. These results also agree with the conclusion that the e^- preservation generated using two co-catalysts could develop the separation of charge carriers and prolong its lifetime, which is beneficial to the memory catalysis after illumination.

On the other hand, according to the result of the Gaussian fitting and previous studies [12,60], a strong fluorescence peak at 520 nm with the excitation of 385 nm, might contribute to the σ mode caused by the longitudinal coupling of the particle plasmons [61]. According to the previous report [62], a dominant single-particle transition ($\Sigma_n \rightarrow \Sigma_{n+1}$) can be identified in the longitudinal peaks. Therefore, longitudinal peaks just could be the evidence of the σ mode. This coupling could promote the transmission of plasmonic charge carriers owing to spatial polarization [13,31]. Moreover, to investigate the donation and transmission of plasmonic e^- at Ag NPs, a quenching experiment was

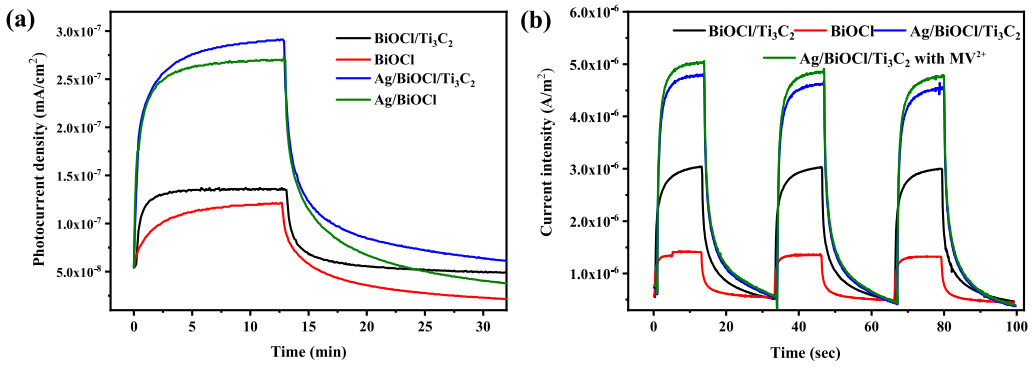

Fig. 6. (a) Long term and (b) short term detection of photo-current response for different as-fabricated samples.

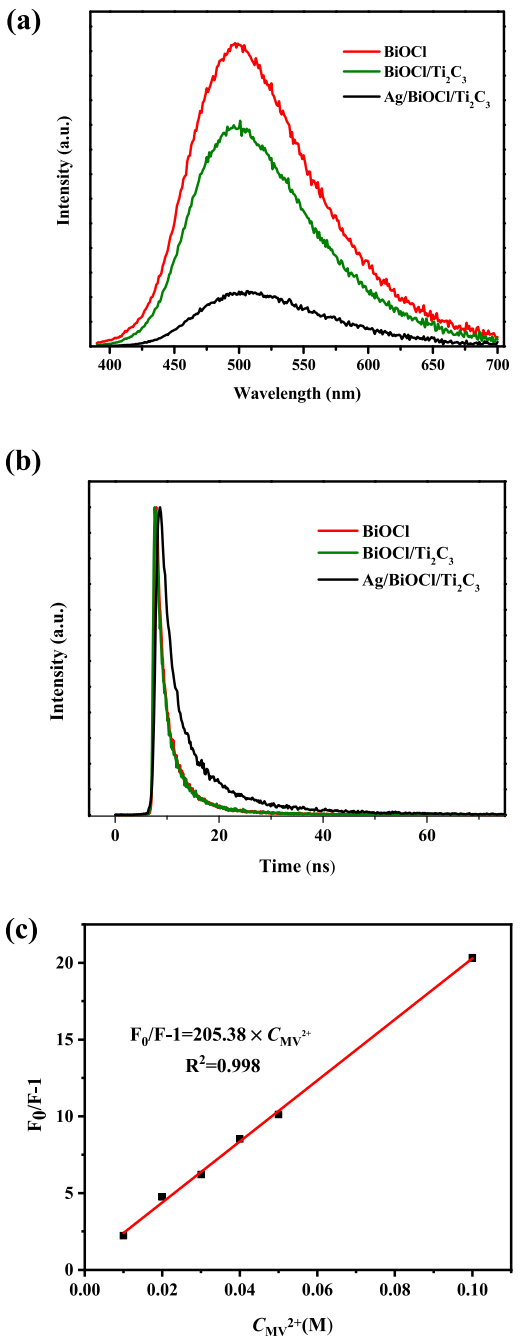

Fig. 7. (a) The steady and (b) time-dependent PL spectra of as-prepared catalyst; (c) Stern – Volmer plot corresponding to the luminescence peak at 510 nm.

conducted introducing MV^{2+}. Fig. 7c, Fig. S7 and Table S4 show that the intensity of the fluorescence peak corresponding to the σ mode was suppressed, which indicates that the e^- donation might exist in the reactive system. With the linear fitting of the Stern–Volmer plot:

$$\frac{F_0}{F} - 1 = K \times C_{MV^{2+}} \tag{11}$$

in which the integrated luminescence intensity of Gaussian fitting was plotted with the MV^{2+} concentration, the constant K was calculated as 205.38 mM^{-1}. This value far exceeded the constant of blank control (6×10^{-7} mM^{-1}), indicating a static rather than dynamic picture. Therefore, an e^- donation process at Ag NPs during the longitudinal coupling of the particle plasmons could be confirmed. For this reason, some extra current and electrons responded gradually to the photo-electric measurements for the ternary sample.

The surface potential of catalysts is shown in Fig. S8. Based on these measurements, the average surface potential of BiOCl, Ti_3C_2/BiOCl, and Ag/BiOCl/Ti_3C_2 was calculated for −0.86 V, −0.92 V, and −1.4 V, respectively. In comparison, BiOCl/Ti_3C_2, and Ag/BiOCl/Ti_3C_2 both displayed more electronegativity [33,63,64]. It suggests that using the combination of Ag NPs and Ti_3C_2 as the electron storage could enhance the electron aggression and deposition on the catalyst surface [17,33]. This negative shift also demonstrates the donor ability in electron transfer owing to the potential energy, which is consisted with the experiments of photo-electric and fluorescence quenching [63,64].

In theory, the LSPR coupling of photocatalyst and plasma in their heterostructures could alter the distribution of the localized electric field and strengthen the intensity of the electron field [65]. To further understand the effect mentioned above, three-dimensional, finite-difference-time-domain (FDTD) simulations were used to illustrate the distribution of hot-charge carriers using the LSPR-induced electric field. Based on the measurement of HRTEM in Fig. 1b, a simplified model was built for further stimulation, shown in Fig. 9a (see Section of *Finite element method simulation* for details). Fig. 8c–d shows that, upon resonance excitation to drive the LSPR coupling of Ag/BiOCl and Ti_3C_2/BiOCl, two different interfaces were used to enhance the localized

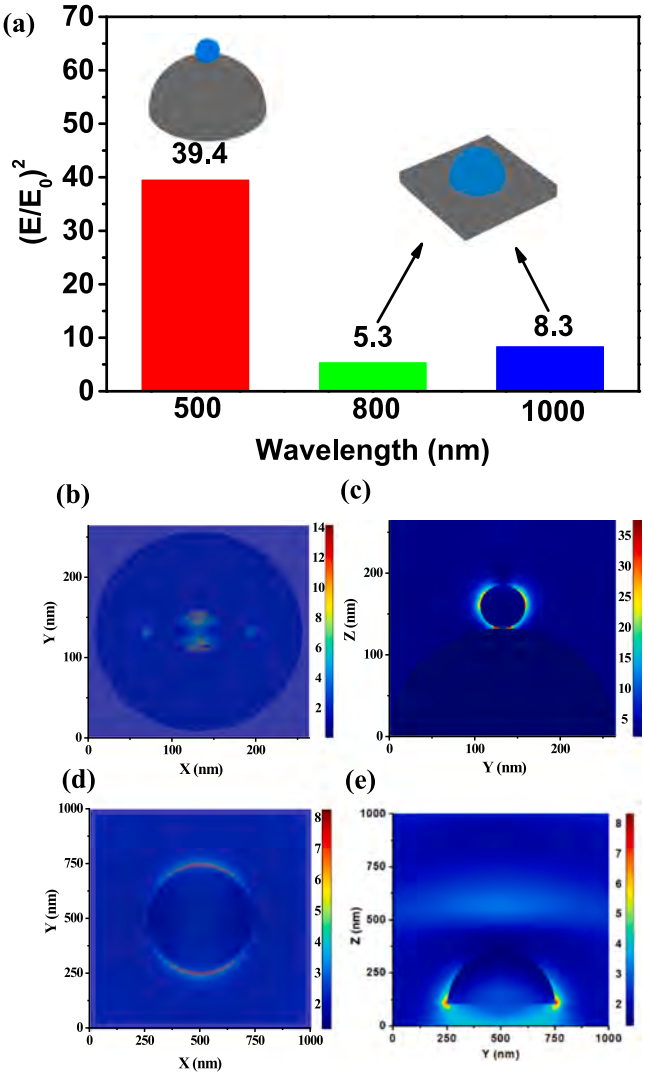

Fig. 8. Simulation results of electric field distributions at different contact-positions excitation for Ag/BiOCl/Ti_3C_2.

electric fields near the plasmonic "hot spot" regions mentioned above. The enhancement factor ($|E|^2/|E_0|^2$) of the electric-field intensity displayed obvious strength with the irradiation of light in three different wavelengths. Specifically, under light (500 nm), $|E|^2/|E_0|^2$ was calculated to be 39.4 at the interface of Ag/BiOCl, while the interface of BiOCl/Ti_3C_2,$|E|^2/|E_0|^2$ also increased by 5.3 and 8.3 under two other illuminative conditions (800 nm and 1000 nm). Owing to the less metallic property, the field enhancement of Ti_3C_2 displayed much lower than metal particles. However, the non-radiated decay from LSPR effect on the Ti_3C_2 surface also promotes the mobility of energetic charge carriers [66]. Combined with the results of UV-vis spectra and simulation, these enhancements confirm that the excitation energy matched the LSPR band well and suggest LSPR-enhanced electric fields were located around the interface of Ag/BiOCl and Ti_3C_2/BiOCl to produce the energetic energetic -charge carriers using the energy adsorption from the incident light. Furthermore, based on the results above, these energetic-charge carriers might be conserved at the Ag NPs and Ti_3C_2 for the next reaction.

3.4.2. *The introduction of extra thermal from energetic-charge carriers using the LSPR effect*

The thermal effect was another enhancing factor for plasmonic photocatalysis, owing to the energetic and active properties of the energetic-charge carriers [21,67]. Therefore, IR thermal images during and after illumination for as-prepared samples were taken to quantify the thermal effect of the memory catalysis. Fig. 9a–c shows that all of the modified samples displayed a thermal effect during irradiation, compared with the single BiOCl. Among these samples, Ag/BiOCl/Ti_3C_2 demonstrated the best performance (42.0 °C), corresponding to the BiOCl/Ti_3C_2 (35.3 °C) and BiOCl (26.1 °C). This remarkable improvement might be the result of the efficient generation of energetic-charge carriers from Ag NPs and Ti_3C_2 plasma, which could introduce much extra energy to the reaction system and consequently boost the activity of memory catalysis in the dark [25,68]. For 5 min after illumination, the surface temperature of Ag/BiOCl/Ti_3C_2 was still as high as 31.6 °C, indicating its more energetic state than with BiOCl/Ti_3C_2 (21.0 °C) and BiOCl (16.7 °C). The slow recession suggests that Ag/BiOCl/Ti_3C_2 has the best performance to preserve heat, which was caused by the deposition of the energetic charge carriers with the excited state at Ag NPs and Ti_3C_2 [25]. This result was similar to that of the long-term, photoelectrical experiment. In general, the experiments with IR thermal images suggested that more energetic-charge carriers were formed by the plasmonic effect on the surface of Ag/BiOCl/Ti_3C_2. After that, some energetic-charge carriers were preserved at Ag NPs and Ti_3C_2, and released slowly in the dark to transform the thermal; this might explain Ag/BiOCl/Ti_3C_2′s best performance for memory catalysis. In order to further investigate the photothermal effect from Ag/BiOCl/Ti_3C_2, the experiment to fit the Arrhenius plot was conducted. Based on the Langmuir-Hinshelwood kinetics model and the temperature-dependent degradation reaction, the Gibbs free energy was 13.3 kJ/mol. This data is much higher than other references, which indicated the active photothermal response could promote the degradation reaction [69].

Combined with all of the results and discussion, two main mechanisms caused by the LSPR and Schottky barriers are summarized in Fig. 10. Under light irradiation, the electron-hole pairs at BiOCl were separated, and then the excited e^- moved from the Bi 6p orbital to the d band of Ag NPs and Ti_3C_2, owing to the formation of Schottky heterojunction. The e^- further changed to energetic-charge carriers located at the 5p and 4p orbital of Ag and Ti atoms, respectively, as a result of the LSPR effect. Because of the e^- donor feature of the two co-catalysts, these energetic-charge carriers could be released gradually for further ROS generation in the dark. On the other hand, the transmission of many energetic-charge carriers caused by the LSPR effect also provides much heat, thus creating the energetic sites for memory catalysis after light irradiation.

4. Conclusions

In this study, a plasmonic catalyst Ag/BiOCl/Ti_3C_2 was fabricated using a multi-step precipitation method. Compared with pure BiOCl and single modification samples (BiOCl/Ti_3C_2 and Ag/BiOCl), this catalyst displayed much enhancement in photocatalytic catalytic performance and memory catalytic activity in degrading tetracycline hydrochloride. The results suggest that the Schottky heterojunction formation and the LSPR generated by Ag NPs and Ti_3C_2 were responsible for its outstanding performance. LSPR could thus promote the absorbance of the light and increase the formation of charge carriers through the involvement of plasmonic energetic-charge carriers. Therefore, more e^- are excited and stored under light and then released to form ROS in the dark. Furthermore, these hot-charge carriers contribute the extra thermal to provide the energy that increases the efficiency of the degradative reaction in both the light and dark. The study is the first to illustrate the synergetic effect of electronic and thermal transfer induced by LSPR on memory catalysis, which will provide new insights into the design of MCs and their practical application in organics removal.

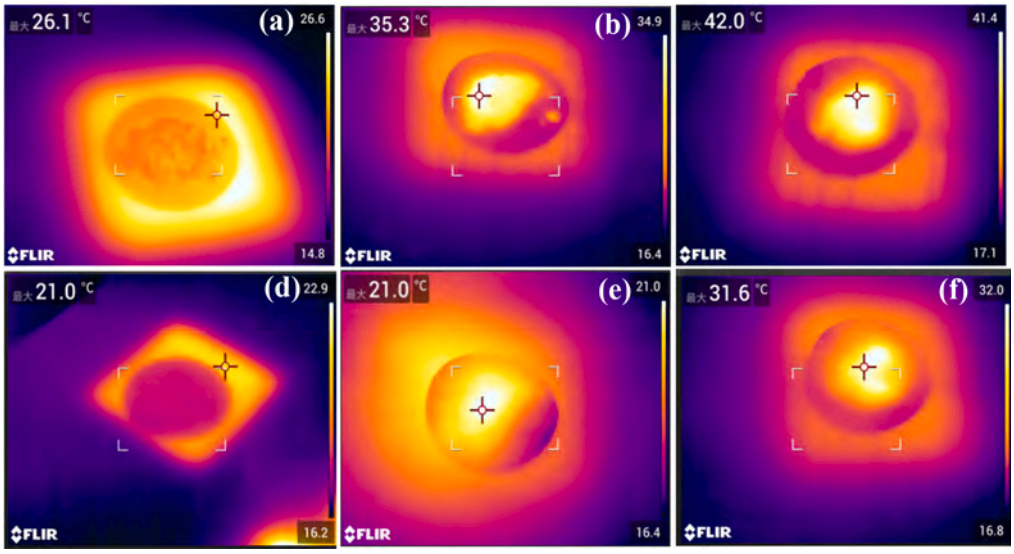

Fig. 9. IR thermal images:(a–c) during the illumination, and (d–f) after the illumination for BiOCl, BiOCl/Ti_3C_2, and Ag/BiOCl/Ti_3C_2, respectively.

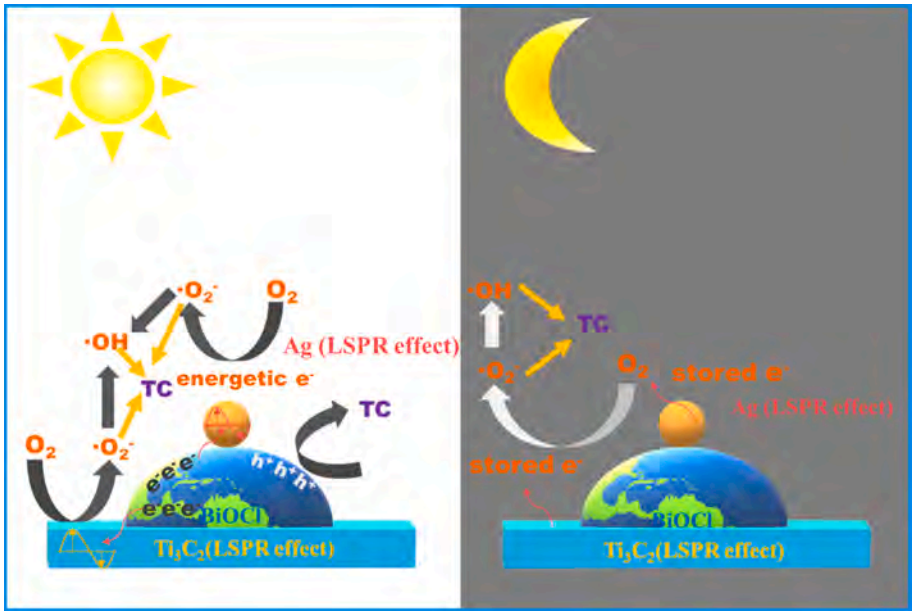

Fig. 10. Schematic illustration of the memory catalysis mechanism.

Declaration of Competing Interest

The authors declare that they have no known competing financial interests or personal relationships that could have appeared to influence the work reported in this paper.

Acknowledgments

The authors acknowledge financial supports from National Natural Science Foundation of China (No. 52000155), the Zhejiang Provincial Natural Science Foundation of China (No. LQ20E080002), and the Public Benefits Projects of Ningbo (No. 202002N3055). We also thank the group of Associate Professor Miaomiao Ye (Zhejiang University) for providing the IR thermal images measurement and the experiment of XRD, XPS and FDTD calculation support from the www.shiyanjia.com.

Appendix A. Supplementary data

Supplementary data to this article can be found online at https://doi.org/10.1016/j.cej.2021.132028.

References

[1] L. Wang, X. Zhang, X. Yu, F. Gao, Z. Shen, X. Zhang, S. Ge, J. Liu, Z. Gu, C. Chen, An All-Organic Semiconductor C_3N_4/PDINH Heterostructure with Advanced Antibacterial Photocatalytic Therapy Activity, Adv. Mater. 31 (33) (2019) 1901965, https://doi.org/10.1002/adma.v31.3310.1002/adma.201901965.
[2] S.-S. Yi, X.-B. Zhang, B.-R. Wulan, J.-M. Yan, Q. Jiang, Non-noble metals applied to solar water splitting, Energy Environ. Sci. 11 (11) (2018) 3128–3156.
[3] H. Liu, H.-L. Jiang, Solar-Powered Artificial Photosynthesis Coupled with Organic Synthesis, Chem 5 (10) (2019) 2508–2510.
[4] M. Sakar, C. Nguyen, M. Vu, T. Do, Materials and Mechanisms of Photo-Assisted Chemical Reactions under Light and Dark Conditions: Can Day-Night Photocatalysis Be Achieved? ChemSusChem 11 (2018) 809–820.
[5] Q.i. Li, Y.W. Li, P. Wu, R. Xie, J.K. Shang, Palladium Oxide Nanoparticles on Nitrogen-Doped Titanium Oxide: Accelerated Photocatalytic Disinfection and Post-Illumination Catalytic "Memory", Adv. Mater. 20 (19) (2008) 3717–3723.
[6] T. Tatsuma, S. Saitoh, Y. Ohko, A. Fujishima, TiO_2-WO_3 photoelectrochemical anticorrosion system with an energy storage ability, Chem. Mat. 13 (9) (2001) 2838–2842.
[7] Y.-H. Chiu, Y.-J. Hsu, Au@Cu_7S_4 yolk@shell nanocrystal-decorated TiO_2 nanowires as an all-day-active photocatalyst for environmental purification, Nano Energy 31 (2017) 286–295.
[8] G. Wang, H. Feng, L. Hu, W. Jin, Q. Hao, A. Gao, X. Peng, W. Li, K. Wong, H. Wang, Z. Li, P. Chu, An antibacterial platform based on capacitive carbon-doped TiO2 nanotubes after direct or alternating current charging, Nat. Commun. 9 (2018) 2055.
[9] V.-H. Lau, D. Klose, H. Kasap, F. Podjaski, M.-C. Pignié, E. Reisner, G. Jeschke, B. V. Lotsch, Dark Photocatalysis: Storage of Solar Energy in Carbon Nitride for Time-Delayed Hydrogen Generation, Angew. Chem.-Int. Edit. 56 (2) (2017) 510–514.
[10] G. Liao, J. Fang, Q. Li, S. Li, Z. Xu, B. Fang, Ag-Based nanocomposites: synthesis and applications in catalysis, Nanoscale 11 (15) (2019) 7062–7096.
[11] Y. Li, Z. Deng, Ag Ion Soldering: An Emerging Tool for Sub-nanomeric Plasmon Coupling and Beyond, Accounts Chem. Res. 52 (12) (2019) 3442–3454.
[12] S. Sheikholeslami, Y.-W. Jun, P.K. Jain, A.P. Alivisatos, Coupling of Optical Resonances in a Compositionally Asymmetric Plasmonic Nanoparticle Dimer, Nano Lett. 10 (7) (2010) 2655–2660.
[13] Y. Choi, M.S. Koo, A.D. Bokare, D.-H. Kim, D.W. Bahnemann, W. Choi, Sequential Process Combination of Photocatalytic Oxidation and Dark Reduction for the Removal of Organic Pollutants and Cr(VI) using Ag/TiO_2, Environ. Sci. Technol. 51 (7) (2017) 3973–3981.
[14] Z. Zeng, X. Quan, H. Yu, S. Chen, Y. Zhang, H. Zhao, S. Zhang, Carbon nitride with electron storage property: Enhanced exciton dissociation for high-efficient photocatalysis, Appl. Catal. B-Environ. 236 (2018) 99–106.
[15] Q.i. Zhang, H. Wang, Z. Li, C. Geng, J. Leng, Metal-Free Photocatalyst with Visible-Light-Driven Post-Illumination Catalytic Memory, ACS Appl. Mater. Interfaces 9 (26) (2017) 21738–21746.
[16] H. Kasap, C.A. Caputo, B.C.M. Martindale, R. Godin, V.-H. Lau, B.V. Lotsch, J. R. Durrant, E. Reisner, Solar-Driven Reduction of Aqueous Protons Coupled to Selective Alcohol Oxidation with a Carbon Nitride-Molecular Ni Catalyst System, J. Am. Chem. Soc. 138 (29) (2016) 9183–9192.
[17] J. Pang, R.G. Mendes, A. Bachmatiuk, L. Zhao, H.Q. Ta, T. Gemming, H. Liu, Z. Liu, M.H. Rummeli, Applications of 2D MXenes in energy conversion and storage systems, Chem. Soc. Rev. 48 (1) (2019) 72–133.
[18] J. Peng, X. Chen, W.-J. Ong, X. Zhao, N. Li, Surface and Heterointerface Engineering of 2D MXenes and Their Nanocomposites: Insights into Electro- and Photocatalysis, Chem 5 (1) (2019) 18–50.
[19] T. Cai, L. Wang, Y. Liu, S. Zhang, W. Dong, H. Chen, X. Yi, J. Yuan, X. Xia, C. Liu, S. Luo, Ag_3PO_4/Ti_3C_2 MXene interface materials as a Schottky catalyst with enhanced photocatalytic activities and anti-photocorrosion performance, Appl. Catal. B-Environ. 239 (2018) 545–554.
[20] S. Cao, B. Shen, T. Tong, J. Fu, J. Yu, 2D/2D Heterojunction of Ultrathin MXene/Bi_2WO_6 Nanosheets for Improved Photocatalytic CO_2 Reduction, Adv. Funct. Mater. 28 (21) (2018) 1800136, https://doi.org/10.1002/adfm.v28.2110.1002/adfm.201800136.
[21] L. Zhou, D.F. Swearer, C. Zhang, H. Robatjazi, H. Zhao, L. Henderson, L. Dong, P. Christopher, E.A. Carter, P. Nordlander, N.J. Halas, Quantifying hot carrier and thermal contributions in plasmonic photocatalysis, Science 362 (6410) (2018) 69–72.
[22] D.F. Swearer, H. Zhao, L. Zhou, C. Zhang, H. Robatjazi, J.M.P. Martirez, C. M. Krauter, S. Yazdi, M.J. McClain, E. Ringe, E.A. Carter, P. Nordlander, N.J. Halas, Heterometallic antenna-reactor complexes for photocatalysis, Proc. Natl. Acad. Sci. U. S. A. 113 (32) (2016) 8916–8920.
[23] Y. Kim, D. Dumett Torres, P.K. Jain, Activation Energies of Plasmonic Catalysts, Nano Lett. 16 (5) (2016) 3399–3407.
[24] S. Eustis, M.A. El-Sayed, Why gold nanoparticles are more precious than pretty gold: Noble metal surface plasmon resonance and its enhancement of the radiative and nonradiative properties of nanocrystals of different shapes, Chem. Soc. Rev. 35 (3) (2006) 209–217.
[25] L.e. Chang, L.V. Besteiro, J. Sun, E.Y. Santiago, S.K. Gray, Z. Wang, A.O. Govorov, Electronic Structure of the Plasmons in Metal Nanocrystals: Fundamental

Limitations for the Energy Efficiency of Hot Electron Generation, ACS Energy Lett. 4 (10) (2019) 2552–2568.
[26] X. Fan, Y. Ding, Y. Liu, J. Liang, Y. Chen, Plasmonic $Ti_3C_2T_x$ MXene Enables Highly Efficient Photothermal Conversion for Healable and Transparent Wearable Device, ACS Nano 13 (7) (2019) 8124–8134.
[27] X. Fan, L.u. Liu, X. Jin, W. Wang, S. Zhang, B. Tang, MXene $Ti_3C_2T_x$ for phase change composite withsuperior photothermal storage capability, J. Mater. Chem. A 7 (23) (2019) 14319–14327.
[28] M.G. Lee, C.W. Moon, H. Park, W. Sohn, S.B. Kang, S. Lee, K.J. Choi, H.W. Jang, Dominance of Plasmonic Resonant Energy Transfer over Direct Electron Transfer in Substantially Enhanced Water Oxidation Activity of $BiVO_4$ by Shape-Controlled Au Nanoparticles, Small 13 (37) (2017) 1701644, https://doi.org/10.1002/smll.v13.3710.1002/smll.201701644.
[29] S.K. Cushing, J. Li, F. Meng, T.R. Senty, S. Suri, M. Zhi, M. Li, A.D. Bristow, N. Wu, Photocatalytic Activity Enhanced by Plasmonic Resonant Energy Transfer from Metal to Semiconductor, J. Am. Chem. Soc. 134 (36) (2012) 15033–15041.
[30] L. Yang, Y. Dall'Agnese, K. Hantanasirisakul, C.E. Shuck, K. Maleski, M. Alhabeb, G. Chen, Y.u. Gao, Y. Sanehira, A.K. Jena, L. Shen, C. Dall'Agnese, X.-F. Wang, Y. Gogotsi, T. Miyasaka, SnO_2-Ti_3C_2 MXene electron transport layers for perovskite solar cells, J. Mater. Chem. A 7 (10) (2019) 5635–5642.
[31] J. Zhang, M. Guan, J. Lischner, S. Meng, O.V. Prezhdo, Coexistence of Different Charge-Transfer Mechanisms in the Hot-Carrier Dynamics of Hybrid Plasmonic Nanomaterials, Nano Lett. 19 (5) (2019) 3187–3193.
[32] H. Huang, Y. Song, N. Li, D. Chen, Q. Xu, H. Li, J. He, J. Lu, One-step in-situ preparation of N-doped TiO_2@C derived from Ti_3C_2 MXene for enhanced visible-light driven photodegradation, Appl. Catal. B-Environ. 251 (2019) 154–161.
[33] T. Cai, Y. Liu, L. Wang, S. Zhang, J. Ma, W. Dong, Y. Zeng, J. Yuan, C. Liu, S. Luo, "Dark Deposition" of Ag Nanoparticles on TiO_2: Improvement of Electron Storage Capacity To Boost "Memory Catalysis" Activity, ACS Appl. Mater. Interfaces 10 (30) (2018) 25350–25359.
[34] V. Strauss, J.T. Margraf, C. Dolle, B. Butz, T.J. Nacken, J. Walter, W. Bauer, W. Peukert, E. Spiecker, T. Clark, D.M. Guldi, Carbon Nanodots: Toward a Comprehensive Understanding of Their Photoluminescence, J. Am. Chem. Soc. 136 (49) (2014) 17308–17316.
[35] X. Jiang, S. Liu, W. Liang, S. Luo, Z. He, Y. Ge, H. Wang, R. Cao, F. Zhang, Q. Wen, J. Li, Q. Bao, D. Fan, H. Zhang, Broadband Nonlinear Photonics in Few-Layer MXene Ti_3C_2Tx (T = F, O, or OH), Laser Photonics Rev. 12 (2) (2018) 1700229, https://doi.org/10.1002/lpor.201700229.
[36] A. Ciesielski, L. Skowronski, M. Trzcinski, T. Szoplik, Controlling the optical parameters of self-assembled silver films with wetting layers and annealing, Appl. Surf. Sci. 421 (2017) 349–356.
[37] L. Zhao, X. Zhang, C. Fan, Z. Liang, P. Han, First-principles study on the structural, electronic and optical properties of BiOX (X=Cl, Br, I) crystals, Physica B: conden. matter 407 (17) (2012) 3364–3370.
[38] L. Chen, X. Ye, S. Chen, L. Ma, Z. Wang, Q. Wang, N. Hua, X. Xiao, S. Cai, X. Liu, Ti_3C_2 MXene nanosheet/TiO_2 composites for efficient visible light photocatalytic activity, Ceram. Inter. 46 (16) (2020) 25895–25904.
[39] Y. Li, L. Ding, Z. Liang, Y. Xue, H. Cui, J. Tian, Synergetic effect of defects rich MoS_2 and Ti_3C_2 MXene as cocatalysts for enhanced photocatalytic H_2 production activity of TiO_2, Chem. Eng. J. 383 (2020) 123178, https://doi.org/10.1016/j.cej.2019.123178.
[40] B. Wang, M. Wang, F. Liu, Q. Zhang, S. Yao, X. Liu, F. Huang, Ti_3C_2: An Ideal Co-catalyst? Angew. Chem.-Int. Edit. 59 (5) (2020) 1914–1918.
[41] Y. Chen, W. Huang, D. He, Y. Situ, H. Huang, Construction of Heterostructured g-C_3N_4/Ag/TiO_2 Microspheres with Enhanced Photocatalysis Performance under Visible-Light Irradiation, ACS Appl. Mater. Interfaces 6 (16) (2014) 14405–14414.
[42] Y. Lin, X. Wu, Y.i. Han, C. Yang, Y. Ma, C. Du, Q. Teng, H. Liu, Y. Zhong, Spatial separation of photogenerated carriers and enhanced photocatalytic performance on Ag_3PO_4 catalysts via coupling with PPy and MWCNTs, Appl. Catal. B-Environ. 258 (2019) 117969, https://doi.org/10.1016/j.apcatb.2019.117969.
[43] P. Makuła, M. Pacia, W. Macyk, How To Correctly Determine the Band Gap Energy of Modified Semiconductor Photocatalysts Based on UV–Vis Spectra, J. Phys. Chem. Lett. 9 (23) (2018) 6814–6817.
[44] S.S. Wu, Y.M. Su, Y.M. Zhang, M.S. Zhu, In-situ growing Bi/BiOCl microspheres on Ti_3C_2 nanosheets for upgrading visible-light-driven photocatalytic activity, Appli. Sur. Sci. 520 (2020), 146339.
[45] H. Wei, A. Reyes-Coronado, P. Nordlander, J. Aizpurua, H. Xu, Multipolar Plasmon Resonances in Individual Ag Nanorice, ACS Nano 4 (5) (2010) 2649–2654.
[46] B. Zheng, X. Wang, C. Liu, K. Tan, Z. Xie, L. Zheng, High-efficiently visible light-responsive photocatalysts: Ag3PO4 tetrahedral microcrystals with exposed 111 facets of high surface energy, J. Mater. Chem. A 1 (40) (2013) 12635, https://doi.org/10.1039/c3ta12946b.
[47] D.C.J. Neo, C. Yang, Y.i. Shi, Q.Y.S. Wu, J. Deng, Y. Xu, A.A. Bettiol, Y. Chan, E. J. Teo, Subwavelength plasmonic color tuning of quantum dot emission, ACS Photonics 6 (1) (2019) 93–98.
[48] R.K. Bommali, D.P. Mahapatra, H. Gupta, P. Guha, D. Topwal, G. Vijaya Prakash, S. Ghosh, P. Srivastava, Angle dependent localized surface plasmon resonance from near surface implanted silver nanoparticles in SiO_2 thin film, J. Appli. phys. 124 (6) (2018) 063107, https://doi.org/10.1063/1.5043386.
[49] M.A. García, J. Llopis, S.E. Paje, A simple model for evaluating the optical absorption spectrum from small Au-colloids in sol-gel films, Chem. Phys. Lett. 315 (5-6) (1999) 313–320.
[50] R.-a. Doong, S.-M. Chang, C.-W. Tsai, Enhanced photoactivity of Cu-deposited titanate nanotubes for removal of bisphenol A, Appl. Catal. B Environ. 129 (2013) 48–55.
[51] Y. Li, W. Zhang, J. Niu, Y. Chen, Mechanism of Photogenerated Reactive Oxygen Species and Correlation with the Antibacterial Properties of Engineered Metal-Oxide Nanoparticles, ACS Nano 6 (6) (2012) 5164–5173.
[52] B. Anasori, M.R. Lukatskaya, Y. Gogotsi, 2D metal carbides and nitrides (MXenes) for energy storage, Nat. Rev. Mater. 2 (2017) 16098.
[53] M. Li, Y. Zhang, X. Li, S. Yu, X. Du, Y. Guo, H. Huang, In-depth insight into facet-dependent charge movement behaviors and photo-redox catalysis: A case of 001 and 010 facets BiOCl, J. Colloid Interf. Sci. 508 (2017) 174–183.
[54] Q.T.H. Ta, E. Cho, A. Sreedhar, J.-S. Noh, Mixed-dimensional, three-level hierarchical nanostructures of silver and zinc oxide for fast photocatalytic degradation of multiple dyes, J. Catal. 371 (2019) 1–9.
[55] T. Kashyap, S. Biswasi, A.R. Pal, B. Choudhury, Unraveling the Catalytic and Plasmonic Roles of g-C_3N_4 Supported Ag and Au Nanoparticles Under Selective Photoexcitation, ACS Sustain. Chem. Eng. 7 (23) (2019) 19295–19302.
[56] S. Bai, X. Li, Q. Kong, R. Long, C. Wang, J. Jiang, Y. Xiong, Toward Enhanced Photocatalytic Oxygen Evolution: Synergetic Utilization of Plasmonic Effect and Schottky Junction via Interfacing Facet Selection, Adv. Mater. 27 (22) (2015) 3444–3452.
[57] J.R. Ran, G.P. Gao, F.T. Li, T.Y. Ma, A.J. Du, S.Z. Qiao, Ti_3C_2 MXene co-catalyst on metal sulfide photo-absorbers for enhanced visible-light photocatalytic hydrogen production, Nat. Commun. 8 (2017) 13907.
[58] Y. Liu, Z. Zhang, Y. Fang, B. Liu, J. Huang, F. Miao, Y. Bao, B. Dong, IR-Driven strong plasmonic-coupling on Ag nanorices/$W_{18}O_{49}$ nanowires heterostructures for photo/thermal synergistic enhancement of H_2 evolution from ammonia borane, Appl. Catal. B-Environ. 252 (2019) 164–173.
[59] H. Wang, S. Jiang, W. Liu, X. Zhang, Q. Zhang, Y.i. Luo, Y.i. Xie, Ketones as Molecular Co-catalysts for Boosting Exciton-Based Photocatalytic Molecular Oxygen Activation, Angew. Chem.-Int. Edit. 59 (27) (2020) 11093–11100.
[60] J. Yuan, W. Guo, E. Wang, Oligonucleotide stabilized silver nanoclusters as fluorescence probe for drug-DNA interaction investigation, Anal. Chim. Acta 706 (2) (2011) 338–342.
[61] P. Nordlander, C. Oubre, E. Prodan, K. Li, M.I. Stockman, Plasmon Hybridization in Nanoparticle Dimers, Nano Lett. 4 (5) (2004) 899–903.
[62] R.D. Senanayake, D.B. Lingerfelt, G.U. Kuda-Singappulige, X. Li, C.M. Aikens, Real-Time TDDFT Investigation of Optical Absorption in Gold Nanowires, J. Phys. Chem. C. 123 (23) (2019) 14734–14745.
[63] R. Chen, S. Pang, H. An, J. Zhu, S. Ye, Y. Gao, F. Fan, C. Li, Charge separation via asymmetric illumination in photocatalytic Cu_2O particles, Nat. Energy 3 (8) (2018) 655–663.
[64] M.J. Shearer, M.-Y. Li, L.-J. Li, S. Jin, R.J. Hamers, Nanoscale Surface Photovoltage Mapping of 2D Materials and Heterostructures by Illuminated Kelvin Probe Force Microscopy, J. Phys. Chem. C 122 (25) (2018) 13564–13571.
[65] Z. Zhang, X. Jiang, B. Liu, L. Guo, N.a. Lu, L.i. Wang, J. Huang, K. Liu, B. Dong, IR-Driven Ultrafast Transfer of Plasmonic Hot Electrons in Nonmetallic Branched Heterostructures for Enhanced H_2 Generation, Adv. Mater. 30 (9) (2018) 1705221, https://doi.org/10.1002/adma.201705221.
[66] M. Spector, A.S. Ang, O.V. Minin, I.V. Minin, A. Karabchevsky, Photonic hook formation in near-infrared with MXene Ti_3C_2 nanoparticles, Nanoscale Adv. 2 (2020) 5312–5318.
[67] K. Wu, J. Chen, J.R. McBride, T. Lian, Efficient hot-electron transfer by a plasmon-induced interfacial charge-transfer transition, Science 349 (6248) (2015) 632–635.
[68] J. Jeon, H. Choi, S. Choi, J.-H. Park, B.H. Lee, E. Hwang, S. Lee, Transition-Metal-Carbide (Mo_2C) Multiperiod Gratings for Realization of High-Sensitivity and Broad-Spectrum Photodetection, Adv. Funct. Mater. 29 (48) (2019) 1905384, https://doi.org/10.1002/adfm.v29.4810.1002/adfm.201905384.
[69] S. Naya, Y. Shite, H. Tada, Hotothermal effect of antimony-doped tin oxide nanocrystals on the photocatalysis, Catal. Commun. 142 (2020), 106044.